npj | Quantum Information

www.nature.com/npjqi

ARTICLE OPEN

Integrated ^{9}Be^{+} multi-qubit gate device for the ion-trap quantum computer

H. Hahn[1,2], G. Zarantonello[1,2], M. Schulte[3], A. Bautista-Salvador[1,2,4], K. Hammerer[3] and C. Ospelkaus[1,2,4]

We demonstrate the experimental realization of a two-qubit Mølmer–Sørensen gate on a magnetic field-insensitive hyperfine transition in ^{9}Be^{+} ions using microwave near-fields emitted by a single microwave conductor embedded in a surface-electrode ion trap. The design of the conductor was optimized to produce a high oscillating magnetic field gradient at the ion position. The measured gate fidelity is determined to be 98.2 ± 1.2% and is limited by technical imperfections, as is confirmed by a comprehensive numerical error analysis. The conductor design can potentially simplify the implementation of multi-qubit gates and represents a self-contained, scalable module for entangling gates within the quantum CCD architecture for an ion-trap quantum computer.

npj Quantum Information (2019)5:70 ; https://doi.org/10.1038/s41534-019-0184-5

INTRODUCTION

Following the proposal by Cirac et al.,[1] trapped atomic ions have shown to be a promising and pioneering platform for implementing elements of quantum information processing (QIP).[2,3] Qubits are encoded in the internal states of individual ions, and shared motional modes are used as a "quantum bus" for multi-qubit operations. Toward a large-scale universal quantum processor based on trapped-ion qubits, the "Quantum Charge-Coupled Device" (QCCD)[4,5] is considered as a possible scalable hardware implementation. It relies on microfabricated multi-zone ion-trap arrays, in which quantum information is processed in dedicated zones interconnected via ion transport. While some key requirements such as high-fidelity ion transport[6] and fault-tolerant single-qubit gates[7,8] have already been demonstrated in multiple setups, high-fidelity multi-qubit gates[9,10] below the fault-tolerant threshold still remain challenging. In this context, entangling gates driven by microwave fields[11,12] represent a technically less demanding alternative to laser-induced gates, as microwave signals can typically be controlled more easily than optical fields from highly specialized laser systems. The microwave approach avoids spontaneous scattering as a fundamental source of infidelities[13] and experimental fidelities[14–17] are approaching the fidelities of the best laser-driven gates.[9,10] Here, we focus on the near-field microwave[12] gate approach, where the leading sources of infidelity in implementations so far comprise the spatio-temporal stability of the microwave near-field pattern[14,18] or fluctuating AC Zeeman shifts.[17,19] We note that in the latter work, the error contribution arising from fluctuating AC Zeeman shifts has been reduced to $\lesssim$0.1% through the use of a dynamical decoupling scheme.[17]

In this letter, we realize a two-qubit gate using a tailored microwave conductor embedded in a surface-electrode trap optimized to produce high oscillating magnetic near-field gradients and low residual fields at the ion position, thus directly addressing the main sources of error in previous near-field gates. The gate is realized on a field-independent hyperfine qubit in ^{9}Be^{+} ions, a promising ion species for scalable QIP,[20–22] following the Mølmer–Sørensen (MS)[23–26] protocol. The implementation is based on an optimized single-conductor design, which can be thought of as the prototype of a scalable multi-qubit gate module for an ion-trap quantum computer based on surface-electrode trap arrays. The measured gate fidelity of 98.2 ± 1.2% is purely limited by technical imperfections, in agreement with a numerical analysis.

RESULTS AND DISCUSSION

The surface-electrode trap was fabricated at the PTB cleanroom facility employing the single-layer method as detailed in ref. [27] on an AlN substrate (for the present trap, we chose the single-layer process in order to quickly test improvements that were made to the setup and trap orientation compared with ref. [28]). Gold electrodes are about 10 μm thick and separated by 5 μm gaps. Aiming to remove potential organic residuals on top of the electrode surfaces, the trap was cleaned in an ex situ dry-etching process before being installed in a UHV vacuum chamber at room temperature. Electrical connectivity is provided by wire bonding to a printed-circuit board for DC signal filtering and signal routing.

Figure 1 shows a top view of the trap center. Besides the microwave conductor MWM, which produces a magnetic field quadrupole[29] suitable for driving multi-qubit gates, the electrode layout includes two microwave conductors labeled MWC to generate an oscillating magnetic field for global spin-state manipulation. The ions are radially and axially confined at an ion-to-electrode distance of about 70 μm using one radio frequency (RF) and 10 DC control electrodes, respectively. With an applied RF voltage of 150V_{pp} at $\Omega_{RF} \simeq 2\pi \times 88.2$ MHz, the motional-mode frequencies of the radial rocking modes of a two-

---

[1]Physikalisch-Technische Bundesanstalt, Bundesallee 100, 38116 Braunschweig, Germany; [2]Institute of Quantum Optics, Leibniz University Hannover, Welfengarten 1, 30167 Hannover, Germany; [3]Institute for Theoretical Physics and Institute for Gravitational Physics (Albert-Einstein-Institute), Leibniz University Hannover, Appelstrasse 2, 30167 Hannover, Germany and [4]Laboratory for Nano- and Quantum Engineering, Leibniz University Hannover, Schneiderberg 39, 30167 Hannover, Germany
Correspondence: C. Ospelkaus (christian.ospelkaus@iqo.uni-hannover.de)

Received: 8 March 2019 Accepted: 26 July 2019

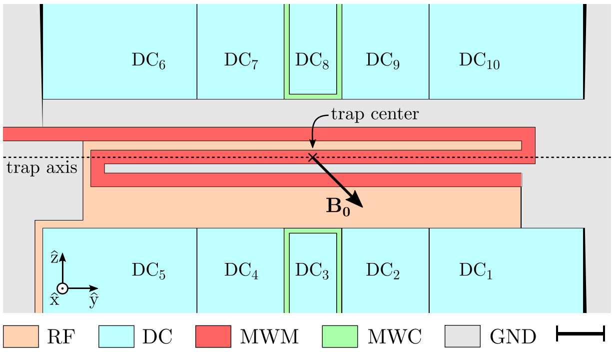

Fig. 1 Electrode configuration around the trap center. The ions are confined 70 µm above the surface using 10 DC control electrodes and one split RF electrode. The microwave conductor labeled MWM produces an oscillating magnetic near-field gradient in the $\hat{x}$–$\hat{z}$ plane in order to drive an entangling gate on two hyperfine qubits. The two microwave conductors labeled MWC can each generate an oscillating magnetic field for global manipulation of the spin state in the $^2S_{1/2}$ manifold. Scale bar: 150 µm (bottom right)

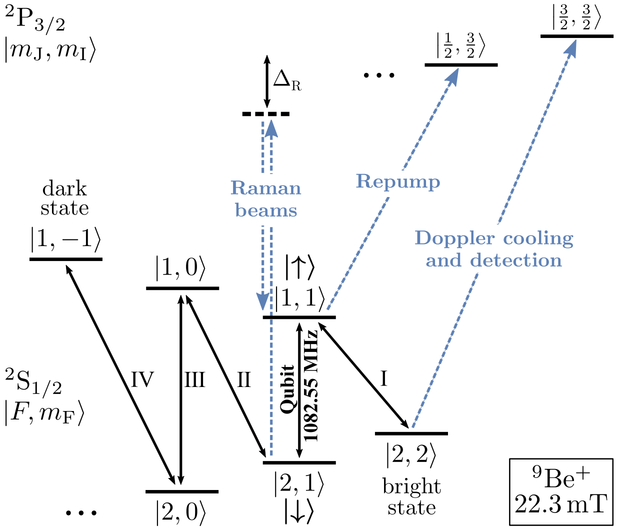

Fig. 2 Relevant energy levels of ^{9}Be$^+$ at 22.3 mT. The transitions indicated as blue dashed lines are addressed by laser beams, while the transitions indicated by black solid lines are driven by microwave radiation. The Raman beam detuning is $\Delta_R \simeq 100$ GHz below the line center of the $^2P_{3/2}$ manifold

ion ^{9}Be$^+$ crystal were measured to be $(\omega_{r1}, \omega_{r2}) \simeq 2\pi \times (6.275, 6.318)$ MHz.

The static magnetic field $\mathbf{B_0}$ defining the quantization axis at an angle of 45° with respect to the trap axis is produced by a hybrid setup consisting of two permanent magnet assemblies and a pair of compensation coils.[30] At the ion position, this setup generates a magnetic field of $|\mathbf{B_0}| = 22.3$ mT forming a first-order magnetic field-insensitive qubit[31] on the hyperfine levels $^2S_{1/2}|F=1, m_F=1\rangle \equiv |\uparrow\rangle$ and $^2S_{1/2}|F=2, m_F=1\rangle \equiv |\downarrow\rangle$ with an unperturbed transition frequency of $\omega_0 \simeq 2\pi \times 1082.55$ MHz, cf. Fig. 2. Here, F and m_F represent the quantum numbers for the ion's total angular momentum and its projection on the quantization axis, respectively.

Ions are loaded using laser ablation combined with photo-ionization.[29] State initialization is done via optical pumping to the $|2, 2\rangle$ state (also referred to as the bright state) and subsequent Doppler cooling on the closed-cycle transition $^2S_{1/2}|2, 2\rangle \leftrightarrow {}^2P_{3/2}|m_J = \frac{3}{2}, m_I = \frac{3}{2}\rangle$ (where m_J and m_I are the projections of the total electronic and nuclear angular momenta onto the quantization axis). Resolved sideband cooling is performed by a pair of counter-propagating Raman beams aligned along the $\hat{z}$ direction. Each sideband cooling cycle consists of a global π rotation on the hyperfine transition labeled "I" in Fig. 2, followed by an optical red sideband pulse on the qubit transition and a repumping sequence to transfer all population back to the initial bright state. The repumping sequence comprises multiple microwave induced π rotations on the qubit transition and laser pulses on the $^2S_{1/2}|1, 1\rangle \leftrightarrow {}^2P_{3/2}|\frac{1}{2}, \frac{3}{2}\rangle$ transition similar to ref. [18] Employing interleaved sideband cooling sequences on both radial rocking modes of a two-ion crystal, we measure a mean phonon number $\bar{n}$ of the modes $\bar{n}_{r1} \simeq 0.27$ and $\bar{n}_{r2} \simeq 0.11$ assuming a thermal distribution. The heating rate was determined to be $\dot{\bar{n}}_{r2} \simeq 28\text{s}^{-1}$. In an earlier measurement with similar radial-mode frequencies, the heating rates of a single-ion's low-frequency (LF) and high-frequency (HF) radial mode were found to be about $\dot{\bar{n}}_{LF} \simeq 116\text{s}^{-1}$ and $\dot{\bar{n}}_{HF} \simeq 122\text{s}^{-1}$, respectively.

To perform a MS two-qubit entangling gate on the qubit transition using near-field microwaves,[12] we subsequently initialize the qubits in $|\uparrow\uparrow\rangle$ and apply a bichromatic microwave current to MWM at the frequencies $\omega_{RSB} = \omega_0 + \Delta - (\omega_{r2} + \delta)$ and $\omega_{BSB} = \omega_0 + \Delta + (\omega_{r2} + \delta)$. Here, δ is the gate detuning from the high-frequency rocking mode of $N = 2$ ions at ω_{r2}, and Δ is the differential AC Zeeman shift of the unperturbed qubit transition induced by the bichromatic field. In the ideal case, the implemented dynamics can be described by the Hamiltonian

$$H_{MS} = \frac{\Omega}{2} \sum_{j=1}^{N} (\sigma_j^+ + \sigma_j^-)(a_{r2} e^{i\delta t} + a_{r2}^\dagger e^{-i\delta t}), \tag{1}$$

where Ω is the gate Rabi frequency, a_{r2} ($a_{r2}^\dagger$) represents the mode's annihilation (creation) operator and we define $\sigma^\pm = 1/2(\sigma^x \pm i\sigma^y)$ with σ^x and σ^y being the Pauli matrices. Following,[32,33] we apply the interaction on $|\uparrow\uparrow\rangle$ in order to produce the maximally entangled state $|\Psi\rangle = 1/\sqrt{2}(|\uparrow\uparrow\rangle + i|\downarrow\downarrow\rangle)$ at time $\tau = \pi\sqrt{K}/\Omega$ (where K is an integer number) and calculate the resulting state preparation fidelity $\mathcal{F} \equiv \langle\Psi|\rho|\Psi\rangle = 1/2(P_{\uparrow\uparrow} + P_{\downarrow\downarrow}) + |\rho_{\uparrow\uparrow,\downarrow\downarrow}|$ by determining the far off-diagonal element $\rho_{\uparrow\uparrow,\downarrow\downarrow}$ of the system's density matrix ρ as well as the population probabilities in $|\downarrow\downarrow\rangle$, $|\uparrow\downarrow\rangle$, and $|\downarrow\uparrow\rangle$, and $|\uparrow\uparrow\rangle$ given by $P_{\downarrow\downarrow}$, $P_{\uparrow\downarrow,\downarrow\uparrow}$, and $P_{\uparrow\uparrow}$, respectively.

Experimentally, we infer these quantities by adding a $\pi/2$ analysis pulse after the gate operation and observe the global ion fluorescence as a function of the analysis pulse's phase ϕ_a employing fluorescence detection on the closed-cycle transition for 400 µs. Prior to detection, we transfer the population in $|\uparrow\rangle$ back to the bright state and shelve the population in $|\downarrow\rangle$ to $|1, -1\rangle$ (also referred to as the dark state) using a sequence of π rotations on the transitions "I" and "II"–"IV", respectively. The populations are determined by repeating the experiment 200 times for each value of ϕ_a, and fitting the resulting histograms to a sum of weighted Poisson distributions representing 0, 1, and 2 ions bright. We calibrate the mean of the distributions to a reference two-ion Ramsey experiment which we assume to produce an ideal outcome following the same procedure of[14] (see Supplementary Methods section). To account for off-resonant optical pumping effects, we modify the three Poissonians to include all depumping processes from the shelved dark state to the bright state during the detection interval.[34] By consequence, we expect the resulting populations to compensate imperfect state preparation and detection within the present level of accuracy. Finally, $\rho_{\uparrow\uparrow,\downarrow\downarrow}$ can be deduced by calculating the parity $\Pi(\phi_a) = P_{\downarrow\downarrow}(\phi_a) + P_{\uparrow\uparrow}(\phi_a) - P_{\uparrow\downarrow+\downarrow\uparrow}(\phi_a)$, while ϕ_a is varied and extracting the magnitude $|A_\Pi|$ of the parity oscillation equal to $|2\rho_{\uparrow\uparrow,\downarrow\downarrow}|$.[33] Figure 3 shows the population and parity signal after performing the two-qubit gate operation using the MWM conductor. From sinusoidal fits to the extracted populations (solid lines), we calculate a corresponding gate fidelity of 98.2 ± 1.2%. The error on the fidelity is derived from

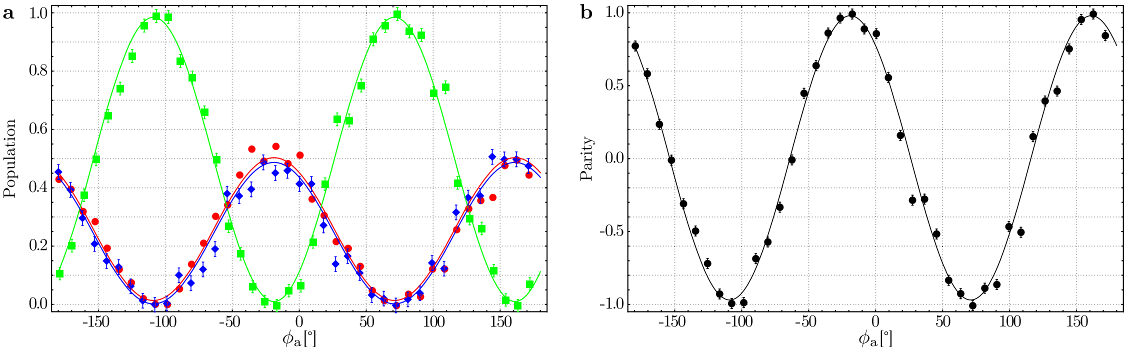

Fig. 3 Population and parity oscillation as a function of the phase ϕ_a of a $\pi/2$ analysis pulse applied after preparing the maximally entangled state $|\Psi\rangle = 1/\sqrt{2}(|\uparrow\uparrow\rangle + \mathrm{i}|\downarrow\downarrow\rangle)$ utilizing the near-field pattern of the MWM conductor. The solid lines are sinusoidal fits to the observed data, while each data point represents the average of 200 experiments. The error bars result from the fit of the weighted Poissonians to the experimental data. **a** Population in $|\downarrow\downarrow\rangle$ ($P_{\downarrow\downarrow}$; red circles), $|\uparrow\downarrow\rangle$ and $|\downarrow\uparrow\rangle$ ($P_{\uparrow\downarrow,\downarrow\uparrow}$; green squares) and $|\uparrow\uparrow\rangle$ ($P_{\uparrow\uparrow}$; blue diamonds). The fits yield $P_{\uparrow\uparrow} + P_{\downarrow\downarrow} = 0.990 \pm 0.021$. **b** Parity $\Pi(\phi_a) = P_{\downarrow\downarrow}(\phi_a) + P_{\uparrow\uparrow}(\phi_a) - P_{\uparrow\downarrow,\downarrow\uparrow}(\phi_a)$ oscillation with a fitted amplitude of $A_\Pi = 0.975 \pm 0.012$

the uncertainties in the population fits. In more detail, we apply a power of ~5.5 W to each sideband tone, resulting in gate Rabi frequency of $\Omega/2\pi = 1.071$ kHz and an inferred near-field gradient of ~19 T m^{-1}. For a single sideband, the corresponding residual magnetic field at the ion position is highly suppressed by the optimized conductor geometry, resulting in an on-resonance Rabi frequency of about $\Omega_c/2\pi$~450 kHz. In case the bichromatic gate drive is applied, the accompanied differential AC Zeeman shift is measured to be $\Delta/2\pi = 4.37$ kHz and is predominantly caused by σ-components of the residual magnetic fields as the induced shifts of the π-components mainly cancel each other assuming an equal power in both sideband tones. In order to suppress off-resonant spin excitations, we adiabatically shape the envelope of the gate pulse at its beginning and end with a 2-μs long cumulative error function using a microwave envelope stabilization circuit based on a fast analog multiplier and a digital PI controller[35] with the regulator setpoint generated by an arbitrary waveform generator.[36] We optimize the gate by fixing the pulse duration to the expected value based on the gate Rabi frequency and subsequently scanning the gate detuning resulting in the highest fidelity. Following this procedure, we find an optimal gate time and detuning of $\tau = 808$ μs and $\delta/2\pi = 3.4$ kHz, respectively, corresponding to $K = 3$ loops in motional-phase space. Here, the mismatch to the theoretically predicted detuning at $\delta_{\mathrm{theory}}/2\pi = 3.71$ kHz was tracked back to a systematic frequency offset from an independent radial-mode frequency measurement as well as a radial mode frequency "chirp" of 0.3 Hz μs^{-1} during the gate pulse. Qualitatively, a similar effect is also observed in other experiments using near-field gradients and appears to be inherent to warm-up processes in the microwave-generating structures.[19] This hypothesis is supported by our observation of a saturation behavior of the "chirp" at ~1 ms. Consequently, we reduce the impact of the "chirp" by preceding the gate with a 400-μs long warm-up pulse with the duration chosen conservatively to avoid excessive heating of trap structures.

In order to identify current infidelity contributions in producing the maximally entangled state, we simulate the dynamics of the system using a master equation considering experimentally determined input parameters. This becomes necessary, as the exact propagator may no longer be obtained analytically in the presence of additional error sources. The master equation is given by

$$\dot{\rho} = -\mathrm{i}[H, \rho] + \mathcal{L}_h\rho + \mathcal{L}_d\rho \tag{2}$$

where the Hamiltonian is $H = \tilde{H}_{\mathrm{MS}} + H_m + H_z + H_{\mathrm{spec}}$, and

$$\tilde{H}_{\mathrm{MS}} = \frac{1}{2}\sum_{j=1}^{N}\left(\Omega^{\mathrm{B}}(t)\sigma_j^+ a_{r2}^\dagger e^{-\mathrm{i}\delta t} + \Omega^{\mathrm{R}}(t)\sigma_j^+ a_{r2} e^{\mathrm{i}\delta t}\right) + \mathrm{H.c.} \tag{3}$$

is an extension to the ideal case presented in Eq. (1). Here, we have assumed equal Rabi frequencies and phases for both ions, which is true in the experiment to the best of our knowledge. Further, $H_{\mathrm{m}} = \delta_\epsilon(t)a_{r2}^\dagger a_{r2}$ describes the instability of the rocking mode frequency, $H_{\mathrm{z}} = \Delta_\epsilon(t)/2\sum_j \sigma_j^z$ gives the uncompensated AC Zeeman shift resulting from shot-to-shot microwave power fluctuations, general Ω^{B} and Ω^{R} allow an imbalance in the two sideband Rabi frequencies, and time dependencies of the pulse shape are taken into account by the time-dependent parameters. Couplings via additional, off-resonant motional modes are included by the term $H_{\mathrm{spec}} = \Omega_{r1}/2\sum_{j=1}^{N}(\sigma_j^+ + \sigma_j^-)(a_{r1}e^{\mathrm{i}(\Delta\nu+\delta)t} + a_{r1}^\dagger e^{-\mathrm{i}(\Delta\nu+\delta)t})$ whereby we limit ourselves to the nearest mode only (with $\Omega_{r1} \simeq \Omega$), which contributes the largest error of this kind. In addition to the unitary dynamics, motional heating to a thermal state with $\overline{n}_{\mathrm{th}} \gg 1$ and qubit decoherence are considered by the Lindblad terms[32] $\mathcal{L}_{\mathrm{h}}\rho = \gamma_{\mathrm{h}}(\mathcal{D}[a_{r2}]\rho + \mathcal{D}[a_{r2}^\dagger]\rho)$ with the heating rate γ_{h} in phonons per second and $\mathcal{L}_{\mathrm{d}}\rho = \gamma_{\mathrm{d}}/2\sum_j \mathcal{D}[\sigma_j^z]\rho$ with the decoherence rate γ_{d}, respectively, where $\mathcal{D}[\hat{O}]\rho = \hat{O}\rho\hat{O}^\dagger - \hat{O}^\dagger\hat{O}\rho/2 - \rho\hat{O}^\dagger\hat{O}/2$.

Table 1 lists contributions of the different error sources to the infidelity $1 - \mathcal{F}$. These values result from numerical simulations of the quantum dynamics according to Eq. (2) considering the ideal gate dynamics with addition of the corresponding noise in the form we described above. All simulations were done with QuTiP[37] and used a truncated Hilbert space for the motional mode. For our analysis, including the first 25 Fock states was sufficient to reach convergence given the low initial thermal distribution and the small motional displacements during the gate.

We examined the following effects, which we considered to be the most relevant, in more detail: the largest error according to our investigation results from the frequency instability of the rocking mode, which establishes the gate dynamics. This effect consists of two parts. On the one hand, normally distributed variations of the frequency with a standard deviation of $\sqrt{\langle(\delta_\epsilon/\delta)^2\rangle} = 1.1 \times 10^{-2}$, inferred from a measured instantaneous linewidth of $2\pi \times 101$ Hz in a calibration scan directly before the gate measurement. On the other hand, a frequency "chirp" within each gate that we model by a linear increase of 0.3 Hz μs^{-1} within the first 600 μs, and subsequent constant frequency leading to in total 1.3% infidelity. While the mode fluctuations can be reduced by actively stabilizing the amplitude and frequency of the trap RF signal,[38,39] the "chirp" can be reduced by e.g., longer warm-up pulses. Simulations (see Fig. 4) also us to identify the individual contribution of each effect in view of further improvements.

The second largest contribution is caused by driving the identical spin–spin interaction via the additional low-frequency

Table 1. Infidelity contributions from different sources of imperfections

Effect	Parameter	Infidelity
Mode instability	$\sqrt{\langle(\delta_\epsilon/\delta)^2\rangle} = 1.1\times 10^{-2}$ 0.3 Hz μs^{-1} "chirp" for 600 μs	1.3×10^{-2}
Spectator mode	$\Delta\nu = 2\pi\times 42.5$ kHz with $\overline{n}_{r1} = 0.27$	5.2×10^{-3}
Motional heating	$\gamma_h = \dot{\overline{n}}_{r2} = 28 s^{-1}$	3.8×10^{-3}
Off-resonant scattering loss	Measured infidelity following refs. [19,43]	$<2.3\times 10^{-3}$
Qubit decoherence	$\tau_d = 1/\gamma_d > 0.5$ s	$<9.3\times 10^{-4}$
Pulse shape	See main text	6.3×10^{-4}
ACZS fluctuations	$\sqrt{\langle(\Delta_\epsilon/\Delta)^2\rangle} = 8\times 10^{-4}$	1.1×10^{-4}
Rabi frequency imbalance	$\frac{\Omega_R-\Omega_B}{\Omega_B} = 2.33\times 10^{-2}$	4.1×10^{-6}

The infidelity values result from numerical simulations of the quantum dynamics according to Eq. (2), including the respective noise effect with a strength given by the measured parameter specified in the second column

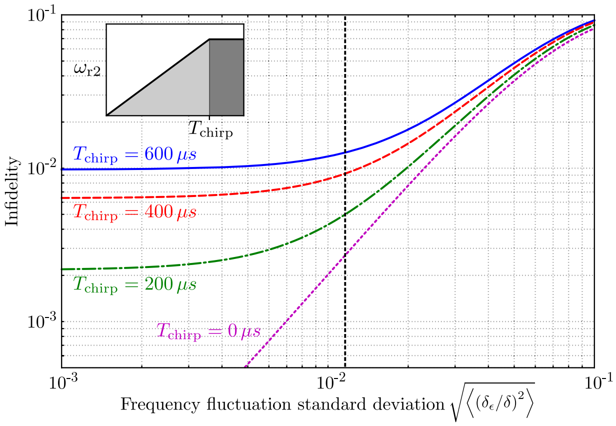

Fig. 4 Simulated infidelity assuming different variations of the relative motional mode frequency and lengths of the frequency "chirp" while considering otherwise ideal gate dynamics. In all cases, the gate parameters are as specified in the text. The experimental condition of the presented two-qubit gate is given by the intersection of the vertical line with the solid blue line. The inset illustrates the observed linear frequency increase of the selected motional mode of about 0.3 Hz μs^{-1} at the beginning of the gate pulse until time T_{chirp}

rocking mode. The measured frequency spacing was $\Delta\nu = \omega_{r2} - \omega_{r1} = 2\pi\times 42.5$ kHz and ground-state cooling to $\overline{n}_{r1} = 0.27$ was applied, resulting in an infidelity of 5.2×10^{-3} from the competing gate dynamics. As this effect scales inversely with the radial-mode splitting, it can be suppressed by engineering the trap potentials or suitable pulse sequences.[40,41] Heating of the motion and decoherence of the qubits contribute ~0.1% and <0.1% infidelity, respectively. Again, both effects do not represent a fundamental limit to the gate performance and can be improved experimentally.[31,42] Off-resonant scattering on carrier transitions can lead to undesired excitations inside and outside the qubit-manifold and thus contribute a gate error. Here, an excitation other than on the qubit transition is much less probable due to the higher-frequency difference of the driving field, which is >150 MHz detuned from the next spectator transition. Direct simulation of this effect was not performed due to the vastly different timescales of the gate dynamics (~kHz) and the carrier processes (~GHz) which would have considerably increased the runtime of the numerical simulations. We instead performed direct measurements on a single qubit[19,43] to evaluate the extent of this error, which is then quantified to be $<2.3\times 10^{-3}$. Infidelities below 6.3×10^{-4} resulted from distortion of the pulse shape, whereby we combine here the influence of adiabatic switching on and off as well as small changes of the Rabi frequency and AC Zeeman shift during the pulses which result from power transients on the ideally rectangular signal. Stabilization of the microwave power allowed to reduce the shot-to-shot fluctuations of the power, and accordingly of the AC Zeeman shift, to an extent that the simulated infidelity of 1.1×10^{-4} contributes only insignificantly. The same applies to the imbalance of Rabi frequencies, cf. Table 1.

In conclusion, we have demonstrated a microwave-driven two-qubit gate with $^9Be^+$ ions using a single microwave conductor with an optimized design embedded in a surface-electrode ion trap. The design of the MWM conductor has been developed to generate a high magnetic near-field gradient with low residual field at the ion position, thus suppressing AC Zeeman shift fluctuations, an inherent error source of the near-field approach, to a simulated infidelity contribution of $\sim 10^{-4}$. In contrast, according to the presented error budget, the main contributions can all be decreased upon technical improvements; the by far biggest of these (1.3%) is consistent with the measured two-qubit gate infidelity of 1.8 ± 1.2%. In addition to technical modifications to the apparatus, more elaborate gate schemes employing Walsh modulation[44] or continuous dynamic decoupling[17] can be applied in order to increase the gate fidelity as required for fault-tolerant quantum computation. In the future, the MWM conductor design can be used as an entangling gate unit of a "QCCD" architecture purely employing microwave-driven quantum gates. Moreover, the conductor design can also be integrated into a scalable multilayer trap.[27,28]

DATA AVAILABILITY

The datasets generated during and/or analyzed during the current study are available from C. Ospelkaus (christian.ospelkaus@iqo.uni-hannover.de) on reasonable request.

ACKNOWLEDGEMENTS

We acknowledge funding from DFG through CRC 1227 DQ-*mat*, projects A01 and A06, and the clusters of excellence "QUEST" and "Quantum Frontiers", from the EU QT flagship project "MicroQC" and from PTB and LUH.

AUTHOR CONTRIBUTIONS

H.H. and G.Z. performed the measurements and analyzed the data. A.B.S. produced the ion trap. M.S. and K.H. contributed the numerical simulations. C.O. devised the experiment plan. All authors participated in the error analysis and the realization of the paper.

ADDITIONAL INFORMATION

Competing interests: The authors declare no competing interests.

REFERENCES

1. Cirac, J. I. & Zoller, P. Quantum computations with cold trapped ions. *Phys. Revi. Lett.* **74**, 4091 (1995).
2. Blatt, R. & Wineland, D. Entangled states of trapped atomic ions. *Nature* **453**, 1008–1015 (2008).
3. Monroe, C. & Kim, J. Scaling the ion trap quantum processor. *Science* **339**, 1164–1169 (2013).
4. Wineland, D. J. et al. Experimental issues in coherent quantum-state manipulation of trapped atomic ions. *J. Res. NIST* **103**, 259–328 (1998).
5. Kielpinski, D., Monroe, C. & Wineland, D. J. Architecture for a large-scale ion-trap quantum computer. *Nature* **417**, 709–711 (2002).

6. Blakestad, R. B. et al. High-fidelity transport of trapped-ion qubits through an X-junction trap array. *Phys. Rev. Lett.* **102**, 153002 (2009).
7. Brown, K. R. et al. Single-qubit-gate error below 10–4 in a trapped ion. *Phys. Rev. A* **84**, 030303 (2011).
8. Harty, T. et al. High-fidelity preparation, gates, memory, and readout of a trapped-ion quantum bit. *Phys. Rev. Lett.* **113**, 220501 (2014).
9. Gaebler, J. et al. High-fidelity universal gate set for Be 9+ ion qubits. *Phys. Rev. Lett.* **117**, 060505 (2016).
10. Ballance, C., Harty, T., Linke, N., Sepiol, M. & Lucas, D. High-fidelity quantum logic gates using trapped-ion hyperfine qubits. *Phys. Rev. Lett.* **117**, 060504 (2016).
11. Mintert, F. & Wunderlich, C. Ion-trap quantum logic using long-wavelength radiation. *Phys. Rev. Lett.* **87**, 257904 (2001).
12. Ospelkaus, C. et al. Trapped-ion quantum logic gates based on oscillating magnetic fields. *Phys. Revi. Lett.* **101**, 090502 (2008).
13. Ozeri, R. et al. Errors in trapped-ion quantum gates due to spontaneous photon scattering. *Phys. Rev. A* **75**, 042329 (2007).
14. Ospelkaus, C. et al. Microwave quantum logic gates for trapped ions. *Nature* **476**, 181–184 (2011).
15. Khromova, A. et al. Designer spin pseudomolecule implemented with trapped ions in a magnetic gradient. *Phys. Rev. Lett.* **108**, 220502 (2012).
16. Weidt, S. et al. Trapped-ion quantum logic with global radiation fields. *Phys. Rev. Lett.* **117**, 220501 (2016).
17. Harty, T. et al. High-fidelity trapped-ion quantum logic using near-field microwaves. *Phys. Rev. Lett.* **117**, 140501 (2016).
18. Warring, U. et al. Techniques for microwave near-field quantum control of trapped ions. *Phys. Rev. A* **87**, 013437 (2013).
19. Sepiol, M. A. *A High-fidelity Microwave Driven Two-qubit Quantum Logic Gate in 43Ca+*. PhD thesis, Oxford (2016).
20. Home, J. P. et al. Complete methods set for scalable ion trap quantum information processing. *Science* **325**, 1227–1230 (2009).
21. Tan, T. R. et al. Demonstration of a dressed-state phase gate for trapped ions. *Phys. Rev. Lett.* **110**, 263002 (2013).
22. Negnevitsky, V. et al. Repeated multi-qubit readout and feedback with a mixed-species trapped-ion register. *Nature* **563**, 527–531 (2018).
23. Sørensen, A. & Mølmer, K. Quantum computation with ions in thermal motion. *Phys. Revi. Lett.* **82**, 1971–1974 (1999).
24. Mølmer, K. & Sørensen, A. Multiparticle entanglement of hot trapped ions. *Phys. Rev. Lett.* **82**, 1835 (1999).
25. Milburn, G., Schneider, S. & James, D. Ion trap quantum computing with warm ions. *Fortschr. Phys.* **48**, 801–810 (2000).
26. Solano, E., de Matos Filho, R. L. & Zagury, N. Deterministic Bell states and measurement of the motional state of two trapped ions. *Phys. Rev. A* **59**, R2539 (1999).
27. Bautista-Salvador, A. et al. Multilayer ion trap technology for scalable quantum computing and quantum simulation. *New J. Phys.* **21**, 043011 (2019).
28. Hahn, H. et al. Multilayer ion trap with three-dimensional microwave circuitry for scalable quantum logic applications. *Appl. Phys. B* **125**, 154 (2019).
29. Wahnschaffe, M. et al. Single-ion microwave near-field quantum sensor. *Appl. Phys. Lett.* **110**, 034103 (2017).
30. Hakelberg, F., Kiefer, P., Wittemer, M., Schaetz, T. & Warring, U. Hybrid setup for stable magnetic fields enabling robust quantum control. *Sci. Rep.* **8**, 4404 (2018).
31. Langer, C. et al. Long-lived qubit memory using atomic ions. *Phys. Rev. Lett.* **95**, 060502 (2005).
32. Sørensen, A. & Mølmer, K. Entanglement and quantum computation with ions in thermal motion. *Phys. Rev. A* **62**, 022311 (2000).
33. Sackett, C. A. et al. Experimental entanglement of four particles. *Nature* **404**, 256–259 (2000).
34. Langer, C. E. *High Fidelity Quantum Information Processing with Trapped Ions*. PhD Thesis, University of Colorado (2006).
35. Hannig, S. et al. A highly stable monolithic enhancement cavity for second harmonic generation in the ultraviolet. *Rev. Sci. Instrum.* **89**, 013106 (2018).
36. Bowler, R., Warring, U., Britton, J. W., Sawyer, B. C. & Amini, J. Arbitrary waveform generator for quantum information processing with trapped ions. *Rev. Sci. Instrum.* **84**, 033108–033108–6 (2013).
37. QuTiP: quantum tool box in PYTHON. http://qutip.org/ (2016).
38. Johnson, K. G. et al. Active stabilization of ion trap radiofrequency potentials. *Rev. Sci. Instrum.* **87**, 053110 (2016).
39. Harty, T. *High-Fidelity Microwave-Driven Quantum Logic in Intermediate-Field 43Ca+*. PhD thesis, Oxford (2013).
40. Choi, T. et al. Optimal quantum control of multimode couplings between trapped ion qubits for scalable entanglement. *Phys. Rev. Lett.* **112**, 190502 (2014).
41. Milne, A. R. et al. Phase-modulated entangling gates robust against static and time-varying errors. Preprint at http://arxiv.org/abs/1808.10462 (2018).
42. Hite, D. A. et al. 100-fold reduction of electric-field noise in an ion trap cleaned with in situ argon-ion-beam bombardment. *Phys. Rev. Lett.* **109**, 103001 (2012).
43. Ballance, C. J. *High-Fidelity Quantum Logic in Ca+*. Springer Theses (Springer International Publishing, Cham, 2017). https://doi.org/10.1007/978-3-319-68216-7.
44. Hayes, D. et al. Coherent error suppression in multiqubit entangling gates. *Phys. Rev. Lett.* **109**, 020503 (2012).